Technical University of Denmark

DTU

Designs for high-efficiency electrically pumped photonic nanowire single-photon sources

Gregersen, Niels; Nielsen, Torben Roland; Mørk, Jesper; Claudon, Julien; Gerard, Jean-Michel

Link back to DTU Orbit

DTU Library
Technical Information Center of Denmark

Designs for high-efficiency electrically pumped photonic nanowire single-photon sources

Niels Gregersen,[1,*] Torben Roland Nielsen,[1] Jesper Mørk,[1] Julien Claudon,[2] and Jean-Michel Gérard[2]

[1]*DTU Fotonik, Department of Photonics Engineering, Technical University of Denmark, Building 343, DK-2800 Kongens Lyngby, Denmark*
[2]*Equipe mixte CEA-CNRS Nanophysique et Semiconducteurs, CEA/INAC/NPSC, 17 rue des Martyrs, 38054 Grenoble Cedex 9, France*
*ngre@fotonik.dtu.dk

Abstract: We propose and analyze three electrically-pumped nanowire single-photon source structures, which achieve output efficiencies of more than 80%. These structures are based on a quantum dot embedded in a photonic nanowire with carefully tailored ends and optimized contact electrodes. Contrary to conventional cavity-based sources, this non-resonant approach provides broadband spontaneous emission control and features an improved fabrication tolerance towards surface roughness and imperfections. Using an element-splitting approach, we analyze the various building blocks of the designs with respect to realistic variations of the experimental fabrication parameters.

©2010 Optical Society of America

OCIS codes: (140.3300) Laser beam shaping; (250.5590) Quantum-well, -wire and -dot devices; (130.2790) Guided waves; (350.4238) Nanophotonics and photonic crystals; (260.3910) Metal optics.

References and Links

1. A. J. Shields, "Semiconductor quantum light sources," Nat. Photonics **1**(4), 215–223 (2007).
2. Z. Yuan, B. E. Kardynal, R. M. Stevenson, A. J. Shields, C. J. Lobo, K. Cooper, N. S. Beattie, D. A. Ritchie, and M. Pepper, "Electrically driven single-photon source," Science **295**(5552), 102–105 (2002).
3. T. Miyazawa, T. Nakaoka, T. Usuki, Y. Arakawa, K. Takemoto, S. Hirose, S. Okumura, M. Takatsu, and N. Yokoyama, "Exciton dynamics in current-injected single quantum dot at 1.55 μm," Appl. Phys. Lett. **92**(16), 161104 (2008).
4. T. Miyazawa, S. Okumura, S. Hirose, K. Takemoto, M. Takatsu, T. Usuki, N. Yokoyama, and Y. Arakawa, "First demonstration of electrically driven 1.55 μm single-photon generator," Jpn. J. Appl. Phys. **47**(4), 2880–2883 (2008).
5. A. Lochmann, E. Stock, O. Schulz, F. Hopfer, D. Bimberg, V. A. Haisler, A. I. Toropov, A. K. Bakarov, and A. K. Kalagin, "Electrically driven single quantum dot polarised single photon emitter," Electron. Lett. **42**(13), 774–775 (2006).
6. C. L. Salter, R. M. Stevenson, I. Farrer, C. A. Nicoll, D. A. Ritchie, and A. J. Shields, "An entangled-light-emitting diode," Nature **465**(7298), 594–597 (2010).
7. T. Heindel, C. Schneider, M. Lermer, S. H. Kwon, T. Braun, S. Reitzenstein, S. Höfling, M. Kamp, and A. Forchel, "Electrically driven quantum dot-micropillar single photon source with 34% overall efficiency," Appl. Phys. Lett. **96**(1), 011107 (2010).
8. J. M. Gérard, B. Sermage, B. Gayral, B. Legrand, E. Costard, and V. Thierry-Mieg, "Enhanced Spontaneous Emission by Quantum Boxes in a Monolithic Optical Microcavity," Phys. Rev. Lett. **81**(5), 1110–1113 (1998).
9. E. Moreau, I. Robert, J. M. Gérard, I. Abram, L. Manin, and V. Thierry-Mieg, "Single-mode solid-state single photon source based on isolated quantum dots in pillar microcavities," Appl. Phys. Lett. **79**(18), 2865–2867 (2001).
10. M. Pelton, C. Santori, J. Vucković, B. Zhang, G. S. Solomon, J. Plant, and Y. Yamamoto, "Efficient source of single photons: a single quantum dot in a micropost microcavity," Phys. Rev. Lett. **89**(23), 233602 (2002).
11. S. Strauf, N. G. Stoltz, M. T. Rakher, L. A. Coldren, P. M. Petroff, and D. Bouwmeester, "High-frequency single-photon source with polarization control," Nat. Photonics **1**(12), 704–708 (2007).
12. W. H. Chang, W. Y. Chen, H. S. Chang, T. P. Hsieh, J. I. Chyi, and T. M. Hsu, "Efficient single-photon sources based on low-density quantum dots in photonic-crystal nanocavities," Phys. Rev. Lett. **96**(11), 117401 (2006).
13. K. J. Vahala, "Optical microcavities," Nature **424**(6950), 839–846 (2003).
14. D. Press, S. Götzinger, S. Reitzenstein, C. Hofmann, A. Löffler, M. Kamp, A. Forchel, and Y. Yamamoto, "Photon antibunching from a single quantum-dot-microcavity system in the strong coupling regime," Phys. Rev. Lett. **98**(11), 117402 (2007).

15. E. Moreau, I. Robert, L. Manin, V. Thierry-Mieg, J. M. Gérard, and I. Abram, "A single-mode solid-state source of single photons based on isolated quantum dots in a micropillar," Physica E **13**(2-4), 418–422 (2002).
16. W. L. Barnes, G. Björk, J. M. Gérard, P. Jonsson, J. A. E. Wasey, P. T. Worthing, and V. Zwiller, "Solid-state single photon sources: light collection strategies," Eur. Phys. J. D **18**(2), 197–210 (2002).
17. A. Naesby, T. Suhr, P. T. Kristensen, and J. Mørk, "Influence of pure dephasing on emission spectra from single photon sources," Phys. Rev. A **78**(4), 045802 (2008).
18. M. Winger, T. Volz, G. Tarel, S. Portolan, A. Badolato, K. J. Hennessy, E. L. Hu, A. Beveratos, J. Finley, V. Savona, and A. Imamoğlu, "Explanation of photon correlations in the far-off-resonance optical emission from a quantum-dot-cavity system," Phys. Rev. Lett. **103**(20), 207403 (2009).
19. A. Auffèves, J. M. Gérard, and J. P. Poizat, "Pure emitter dephasing: A resource for advanced solid-state single-photon sources," Phys. Rev. A **79**(5), 053838 (2009).
20. U. Hohenester, A. Laucht, M. Kaniber, N. Hauke, A. Neumann, A. Mohtashami, M. Seliger, M. Bichler, and J. Finley, "Phonon-assisted transitions from quantum dot excitons to cavity photons," Phys. Rev. B **80**(20), 201311 (2009).
21. J. P. Zhang, D. Y. Chu, S. L. Wu, S. T. Ho, W. G. Bi, C. W. Tu, and R. C. Tiberio, "Photonic-wire laser," Phys. Rev. Lett. **75**(14), 2678–2681 (1995).
22. G. Lecamp, P. Lalanne, and J. P. Hugonin, "Very large spontaneous-emission β factors in photonic-crystal waveguides," Phys. Rev. Lett. **99**(2), 023902 (2007).
23. T. Lund-Hansen, S. Stobbe, B. Julsgaard, H. Thyrrestrup, T. Sünner, M. Kamp, A. Forchel, and P. Lodahl, "Experimental realization of highly efficient broadband coupling of single quantum dots to a photonic crystal waveguide," Phys. Rev. Lett. **101**(11), 113903 (2008).
24. Y. C. Jun, R. M. Briggs, H. A. Atwater, and M. L. Brongersma, "Broadband enhancement of light emission in silicon slot waveguides," Opt. Express **17**(9), 7479–7490 (2009).
25. V. S. C. Manga Rao, and S. Hughes, "Single quantum-dot Purcell factor and β factor in a photonic crystal waveguide," Phys. Rev. B **75**(20), 205437 (2007).
26. I. Friedler, C. Sauvan, J. P. Hugonin, P. Lalanne, J. Claudon, and J. M. Gérard, "Solid-state single photon sources: the nanowire antenna," Opt. Express **17**(4), 2095–2110 (2009).
27. A. V. Maslov, M. I. Bakunov, and C. Z. Ning, "Distribution of optical emission between guided modes and free space in a semiconductor nanowire," J. Appl. Phys. **99**(2), 024314 (2006).
28. J. Claudon, J. Bleuse, N. S. Malik, M. Bazin, P. Jaffrennou, N. Gregersen, C. Sauvan, P. Lalanne, and J. M. Gérard, "A highly efficient single-photon source based on a quantum dot in a photonic nanowire," Nat. Photonics **4**(3), 174–177 (2010).
29. T. M. Babinec, B. J. M. Hausmann, M. Khan, Y. Zhang, J. R. Maze, P. R. Hemmer, and M. Lončar, "A diamond nanowire single-photon source," Nat. Nanotechnol. **5**(3), 195–199 (2010).
30. H. C. Casey, D. D. Sell, and K. W. Wecht, "Concentration dependence of the absorption coefficient for n- and p-type GaAs between 1.3 and 1.6 eV," J. Appl. Phys. **46**(1), 250–257 (1975).
31. S. Gehrsitz, F. K. Reinhart, C. Gourgon, N. Herres, A. Vonlanthen, and H. Sigg, "The refractive index of $Al_xGa_{1-x}As$ below the band gap: Accurate determination and empirical modeling," J. Appl. Phys. **87**(11), 7825–7837 (2000).
32. M. A. Ordal, L. L. Long, R. J. Bell, S. E. Bell, R. R. Bell, R. W. Alexander, Jr., and C. A. Ward, "Optical properties of the metals Al, Co, Cu, Au, Fe, Pb, Ni, Pd, Pt, Ag, Ti, and W in the infrared and far infrared," Appl. Opt. **22**(7), 1099–20 (1983).
33. C. Coutal, A. Azéma, and J.-C. Roustan, "Fabrication and characterization of ITO thin films deposited by excimer laser evaporation," Thin Solid Films **288**(1-2), 248–253 (1996).
34. T. Hanemann, J. Böhm, K. Honnef, E. Ritzhaupt-Kleissl, and J. Haußelt, "Polymer/Phenanthrene-Derivative Host-Guest Systems: Rheological, Optical and Thermal Properties," Macromol. Mater. Eng. **292**(3), 285–294 (2007).
35. T. Bååk, "Silicon oxynitride; a material for GRIN optics," Appl. Opt. **21**(6), 1069–1072 (1982).
36. Y.-R. Nowicki-Bringuier, R. Hahner, J. Claudon, G. Lecamp, P. Lalanne, and J. M. Gérard, "A novel high-efficiency single-mode single photon source," Ann. Phys. (France) **32**(2-3), 151–154 (2007).
37. I. Friedler, P. Lalanne, J. P. Hugonin, J. Claudon, J. M. Gérard, A. Beveratos, and I. Robert-Philip, "Efficient photonic mirrors for semiconductor nanowires," Opt. Lett. **33**(22), 2635–2637 (2008).
38. N. Gregersen, T. R. Nielsen, J. Claudon, J. M. Gérard, and J. Mørk, "Controlling the emission profile of a nanowire with a conical taper," Opt. Lett. **33**(15), 1693–1695 (2008).
39. C. Böckler, S. Reitzenstein, C. Kistner, R. Debusmann, A. Löffler, T. Kida, S. Höfling, A. Forchel, L. Grenouillet, J. Claudon, and J. M. Gérard, "Electrically driven high-Q quantum dot-micropillar cavities," Appl. Phys. Lett. **92**(9), 091107 (2008).
40. P. Bienstman, and R. Baets, "Optical modelling of photonic crystals and VCSELs using eigenmode expansion and perfectly matched layers," Opt. Quantum Electron. **33**(4/5), 327–341 (2001).
41. N. Gregersen, and J. Mørk, "An Improved Perfectly Matched Layer for the Eigenmode Expansion Technique," Opt. Quantum Electron. **40**(11-12), 957–966 (2008).
42. N. Gregersen, T. R. Nielsen, B. Tromborg, and J. Mørk, "Quality factors of nonideal micro pillars," Appl. Phys. Lett. **91**, 011116 (2007).
43. M. Karl, B. Kettner, S. Burger, F. Schmidt, H. Kalt, and M. Hetterich, "Dependencies of micro-pillar cavity quality factors calculated with finite element methods," Opt. Express **17**(2), 1144–1158 (2009).
44. Y. Zhang, and M. Lončar, "Submicrometer diameter micropillar cavities with high quality factor and ultrasmall mode volume," Opt. Lett. **34**(7), 902–904 (2009).

45. D. Englund, H. Altug, and J. Vučković, "Low-threshold surface-passivated photonic crystal nanocavity laser," Appl. Phys. Lett. **91**(7), 071124 (2007).
46. R. B. Patel, A. J. Bennett, K. Cooper, P. Atkinson, C. A. Nicoll, D. A. Ritchie, and A. J. Shields, "Postselective two-photon interference from a continuous nonclassical stream of photons emitted by a quantum dot," Phys. Rev. Lett. **100**(20), 207405 (2008).
47. A. J. Bennett, R. B. Patel, C. A. Nicoll, D. A. Ritchie, and A. J. Shields, "Interference of dissimilar photon sources," Nat. Phys. **5**(10), 715–717 (2009).
48. J. P. Reithmaier, G. Sęk, A. Löffler, C. Hofmann, S. Kuhn, S. Reitzenstein, L. V. Keldysh, V. D. Kulakovskii, T. L. Reinecke, and A. Forchel, "Strong coupling in a single quantum dot-semiconductor microcavity system," Nature **432**(7014), 197–200 (2004).
49. K. Sanaka, A. Pawlis, T. D. Ladd, K. Lischka, and Y. Yamamoto, "Indistinguishable photons from independent semiconductor nanostructures," Phys. Rev. Lett. **103**(5), 053601 (2009).

1. Introduction

The development of solid-state single-photon sources (SPSs) is a major challenge in the context of quantum communication, optical quantum information processing, and metrology [1]. Ideally, such a source must implement a stable single-photon emitter with a high radiative yield. For practical reasons, it is also highly desirable to trigger the single-photon emission by an electrical pulse. In this context, a semiconductor quantum dot (QD) is an attractive single-photon emitter, which has a nearly perfect radiative yield and a stable emission (no blinking or bleaching). Moreover, it benefits from the maturity of semiconductor technology and can be incorporated into the intrinsic region of a *p-i-n* structure, to realize a single-photon LED [2–7].

For all potential applications, the efficiency ε of the source, defined here as the probability to collect a photon into the first lens of the optical setup, is a key figure of merit. Unfortunately, for a QD embedded in a semiconductor material, the large refractive index of the semiconductor prevents an efficient photon extraction and limits ε to below a few percent. The collection of photons can be strongly improved by inserting the QD in a resonant optical microcavity and, up to very recently, this strategy has provided the most efficient SPS. Thanks to their spectrally-narrow emission lines at cryogenic temperatures, the spontaneous emission (SE) of QDs can be controlled through cavity quantum electrodynamical effects. The Purcell effect that arises when a QD is inserted in a resonant optical microcavity with a high-quality factor (Q) and low-volume dynamically funnels a fraction β of its SE into the cavity mode [8–12]. The photon then escapes through a specifically designed loss channel to be collected by external optics with a probability γ. In this simple picture, the photon outcoupling efficiency ε_0 is given by $\varepsilon_0 = \eta\beta\gamma$, where η the radiative quantum efficiency of the QD exciton. The total source efficiency reads $\varepsilon = \varepsilon_0\xi$, where ξ is the pumping efficiency (defined here as the probability to inject at least one electron-hole pair in the QD per command pulse). In the past few years, fabrication progress has led to an impressive improvement of the microcavity figures of merit [13] which in turn brought β close to 100% [14], while η is usually close to 100% for self-assembled QDs at low temperature. However, ε remains so far limited to about 44% [10,11,15] for optically pumped SPSs and 34% for electrically pumped devices [7].

In fact, the far-field emission pattern of high-Q cavities is very sensitive to fabrication imperfections [16]. Thus, defects scatter photons in random directions, which limits γ. The issue is even more serious for electrically pumped structures, which require doping and contact electrodes, potential sources of additional optical losses. Moreover, combining a high efficiency with pure single-photon emission is desirable for most SPS applications. Under non-resonant optical pumping [10,11] or electrical pumping [7], most of the cavity-based SPSs exhibit an autocorrelation function at zero time delay $g^{(2)}(\tau = 0)$ well above 0, when the QD is saturated. The origin of the detrimental multiphoton pulses under strong pumping is not yet fully elucidated. It could be related to non-resonant cavity feeding [17–20] or recapture of carriers if the injection of electrons and holes in the dot is not fast enough compared to the QD radiative decay. Finally, the exploitation of the Purcell effect is restricted to quasi-monochromatic emitters and is effective only over the narrow bandwidth of the cavity resonance.

In this context, the non-resonant SE control provided by a one-dimensional photonic system [21–25] constitutes an appealing alternative to cavity designs. Recently, an optically pumped source design, relying on an InAs QD embedded in a GaAs photonic nanowire was proposed [26]. This geometry ensures a broadband and nearly perfect SE control for an emitter located on the wire axis; β exceeds 90% in a 200 nm wavelength range and features a reasonable tolerance towards off-axis positioning [27]. Moreover, an additional optimization of the far-field emission, using a SiO_2-gold mirror and a smooth tapering of the upper extremity of the wire, led to a record-high measured efficiency of 72% [28]. The broadband SE control in photonic wires has also been recently used to demonstrate a 40% SPS efficiency at room temperature for a color center embedded in a diamond photonic nanowire [29].

In this work, we investigate the feasibility of high efficiency, electrically pumped, SPSs based on a quantum dot in the photonic nanowire geometry. Our focus is the photon extraction efficiency of the SPS, and we assume in the following that $\xi = \eta = 1$ and thus $\varepsilon = \varepsilon_0 = \beta\gamma$. Possible deviations from this ideal situation are discussed in section 6 of the paper. The InAs/GaAs material system, which is the most technologically mature and studied system, is chosen. The paper addresses in particular the associated issue of charge injection electrodes compatible with efficient photon extraction. We investigate three different structures, one inspired by Ref [26]. and two new designs that we believe more adapted to the realization of a practical, electrically pumped source.

The paper is organized as follows. In section 2 we describe the three electrically pumped structures that are analyzed in the paper. In section 3 we present the simplified model based on an element-splitting approach employed to determine the efficiency. We analyze the performance of the various elements of the structures in section 4. Initial experimental results, which confirm the technological feasibility of these designs, are presented in section 5. A discussion of the predicted efficiencies follows in section 6, and finally a conclusion and an outlook are given in section 7.

2. Nanowire SPS structures

In the following we study the GaAs nanowire with an embedded InAs QD emitting light at a wavelength of $\lambda = 950$ nm, and all subsequent computations are performed at this wavelength. We assume that the QD is positioned in the center of the nanowire and has an in-plane dipole orientation. The QD is approximated with a point dipole and we neglect the small perturbation induced by the refractive index profile of the finite size QD on the mode properties of the waveguide structures. We investigate the three electrically pumped SPS designs illustrated in Fig. 1.

All the designs are rotationally symmetric. The materials used are GaAs, Si_3N_4, polymer, gold and indium-tin-oxide (ITO). The polymer electrically isolates the contact sections and the GaAs nanowire is doped to create a *p-i-n* diode. The refractive indices of the materials employed in our simulations are given in Table 1. An absorption loss of $\kappa = 10$ cm^{-1} in the inverted tapers of designs B and C due to free-carrier scattering from *n*-doping with a carrier concentration of ~10^{18} cm^{-3} [30] is included. The doping concentration may be increased locally near the contacts to ensure good electrical conductivity, however we do not expect local doping to have a major influence on the calculated losses in the tapers.

An optically pumped nanowire single-photon source design featuring a nanowire, a conical taper and a bottom metal mirror was described in Ref [26], and the design A represents the most simplistic extension of this design to accommodate electrical pumping. It features a nanowire with a quantum dot in section I ensuring a high β [36], a bottom mirror in section II reflecting light emitted towards the substrate [37], a regular conical tapering in section III-A for controlling the far field radiation pattern [38] and a top contact region in section IV-A.
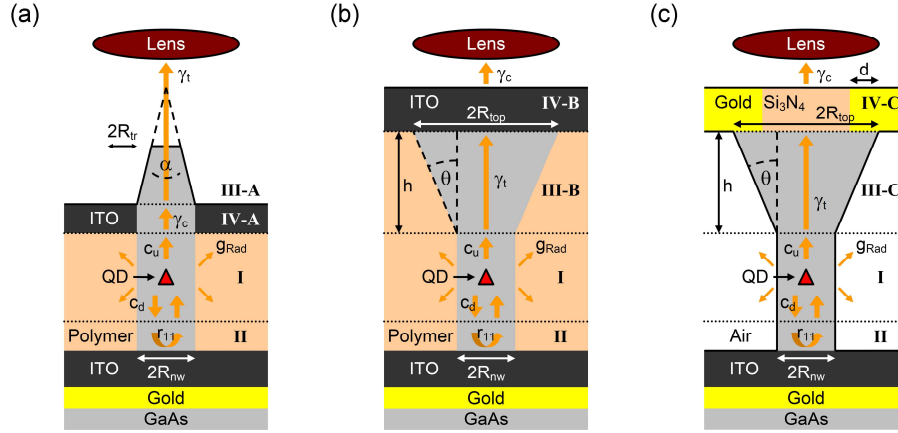
Fig. 1. Design A (a) featuring a top conical tapering and designs B (b) and C (c) with inverted tapering and anti-reflection coatings. Design B features a planar ITO top contact while design C includes a gold ring contact and an air pocket.

Table 1. Material refractive indices.

Material	Refractive index	Reference
GaAs	3.54	[31]
GaAs (*n*-doped taper)	$3.54 + \kappa\lambda/4i$	[30], [31]
Gold	$0.19 + 6.1i$	[32]
ITO	$1.75 + 0.02i$	[33]
Polymer (UP)	1.57	[34]
Si_3N_4	1.99	[35]

In Ref [26]. the metal in the bottom mirror in section II is silver and a thin SiO_2 layer is sandwiched between the nanowire and the metal to improve the reflectivity [37]. For electrical pumping, we replace the electrically isolating SiO_2 layer with a conducting ITO layer, and, to avoid the rapid oxidation of silver in air, we replace silver by a gold bottom layer which is used for the bottom electrical contact. For the top electrical contact in section IV-A we choose ITO instead of gold, as the fundamental mode of the nanowire extends into the cladding material and propagation through a gold cladding results in a large loss reducing efficiency.

While the design A is conceptually simple, the fabrication of the side top contact without damaging the conical taper poses an experimental challenge. For this reason we propose the designs B and C, where well-established technology [7,39] from micropillar SPSs is employed for the top contact.

The design B features the same nanowire and bottom metal mirror sections I and II, however the strategy for controlling the far field radiation pattern is based on the inverse taper of section III-B rather than a regular conical one. In this design, the fundamental mode is adiabatically expanded inside the taper, which also guides electrical current to the quantum dot. The contact section IV-B consists of an easily deposited uniform layer of ITO serving the dual purpose as a top contact and an anti-reflection coating.

Finally, we propose the design C, where a gold ring slightly overlapping the GaAs cylinder is employed for the top contact [7,39]. The gold contact also scatters the fundamental mode, but for small *d* and large R_{top}, this scattering can be negligible. The design C also features an air pocket surrounding the QD nanowire section. This air pocket leads to an increased index contrast and thus a higher *β*. These effects are further analyzed and discussed below.

Combinations of the elements from the designs B and C, e.g. a top ITO planar contact with an air pocket, can also be imagined.

3. SPS efficiency in the element-splitting approach

To determine the SPS efficiency ε we should place the point dipole inside the full structure and compute the corresponding far field emission. Though this approach is rigorous, it does not give a clear physical insight into the physical mechanisms governing the efficiency. For this reason we instead employ a single-mode model based on an element-splitting approach. This simplified model, the validity of which was demonstrated in Ref [26], allows us to analyze and optimize the various elements separately.

The model includes two approximations. First we assume that light scattered out of the fundamental mode into higher-order modes is not coupled back to the fundamental mode and does not reach the collection optics. This is a good approximation for a high-efficiency SPS, where the coupling of the HE_{11} mode to higher-order modes is weak. Second, we assume that the SE rate into radiation modes, g_{Rad}, for the full structure is identical to that for the isolated nanowire element I. This assumption will be justified by the agreement of the results from the simplified model with those obtained using an exact computation, as shown later.

We consider the propagation of the fundamental HE_{11} mode in the full SPS structure, illustrated in Fig. 1 above. The coefficient r_{11}, describes the amplitude reflection cofficient of the bottom mirror, and γ_t and γ_c are intensity transmission coefficients of the HE_{11} mode in the corresponding taper and contact sections. The amplitude coefficients of the upward and downward propagating fundamental mode at the position of the QD are denoted c_u and c_d. The total efficiency ε is given by

$$\varepsilon = \frac{|c_u|^2 \gamma}{g_{Total}},\tag{1}$$

where $\gamma = \gamma_t \gamma_c$ and g_{Total} is the total emission rate. For the QD in the infinitely long nanowire the amplitude coefficients are given by $c_u = c_d = c_0 \circ \text{sqrt}(g_{HE11} / 2)$, where g_{HE11} is the SE rate into the fundamental mode. In the presence of the metal mirror we still have $c_d = c_0$, however the coefficient c_u is modified to include the reflection of the downward propagating mode such that

$$c_u = c_0 \left(1 + |r_{11}| e^{i\phi}\right).\tag{2}$$

Here, φ is the total phase change for the downward propagating reflected mode, however we will assume that the QD is placed in an antinode of the optical field such that $\varphi = 0$. The total SE rate g_{Total} is given by

$$g_{Total} = |c_u|^2 + \left(1 - |r_{11}|^2\right)|c_d|^2 + g_{Rad}.\tag{3}$$

Insertion of Eqs. (2) and (3) in Eq. (1) and using $\beta = g_{HE11} / (g_{HE11} + g_{Rad})$ results in

$$\varepsilon = \frac{\beta \gamma \left(1 + |r_{11}|\right)^2}{2\left(1 + \beta |r_{11}|\right)}.\tag{4}$$

Equation (4) is a transparent expression for the total efficiency ε. The element-splitting approach thus allows us to analyze the four building blocks separately and directly study the influence of the characteristic parameters β, r_{11}, γ_t and γ_c on the SPS efficiency ε.

4. Element analysis

We discuss the performance of the various elements in the following subsections. These studies subsequently allow us to determine the total efficiency coefficient ε using our simplified model based on the element-splitting approach.

The numerical simulations have been performed using the eigenmode expansion technique (EET) [40] with improved perfectly matched layers [41], and the tapering sections of elements IV and V are modelled using a staircase approximation [42].

The analysis of the various elements mainly consists of computing scattering coefficients for the eigenmodes, and the EET directly produces scattering matrices relating incoming and outgoing modes. Even though the staircase approximation is less elegant than the modeling of a tapered section performed in Ref [43], the extraction of scattering coefficients from the finite elements method or the finite-difference time-domain technique is not immediate, and the EET thus remains a natural choice for analyzing the separate building blocks.

Element I: QD section

The first element is the GaAs nanowire with an embedded QD surrounded by a cladding material illustrated in Fig. 2(a). We here study the β factor, that is the power coupled to the fundamental mode relative to total power radiated by the QD. To this purpose we approximate the QD with an in-plane oriented dipole placed in the center. For a radially oriented emitter closer to the center than the sidewalls, values of β larger than 75% are expected [27], however a detailed study of the influence of the position of the QD in the nanowire is beyond this work. We now compute the SE power emission rate g_{HE11} into the fundamental mode as well as the rate g_{Rad} into radiation modes. The total SE rate is then given by $g_{Total} = g_{HE11} + g_{Rad}$, and in Fig. 2(b) we plot $\beta = g_{HE11} / g_{Total}$ as function of R_{nw} for various cladding indices.
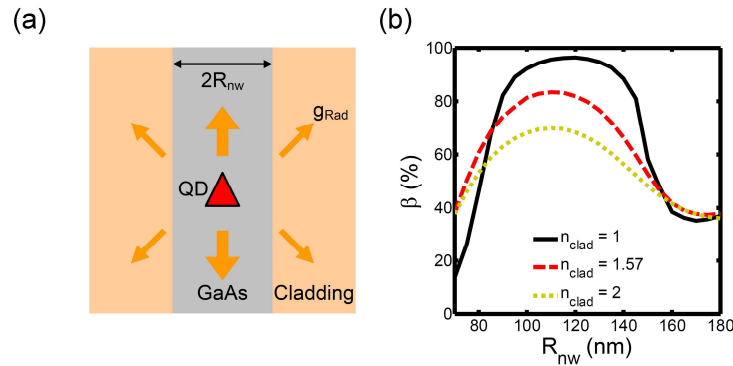

Fig. 2. Sketch of element I (a) and β as function of nanowire radius R_{nw} (b) for various cladding refractive indices n_{clad}.

We observe in Fig. 2(b) that the maximum value of β depends on the index contrast. To understand this dependence we note that the high β value is the result of a screening effect, which dampens the field amplitude of radiation modes inside the nanowire. The magnitude of the effect is proportional to the index contrast between core and cladding. For the nanowire surrounded by air, we obtain a β value of 96.3% for a R_{nw} ~120 nm, while in the geometry with polymer cladding ($n_{clad} = 1.57$) the index contrast is smaller and the maximum β value is reduced to 83.3% for R_{nw} ~110 nm. In the following we consider these two parameter sets for designs A and B and design C, respectively.

Regarding the height of element I, the only requirement to maintain SE control is $\varphi = 0$ in (2). With this condition met, the distance between the emitter and the adjacent elements should be minimized to reduce electrical and optical losses.

Element II: Metal mirror

Choosing the correct nanowire radius R_{nw} ensures a high β value, however half of the generated photons still propagate towards the substrate and to achieve high efficiency a bottom mirror with a high reflection coefficient of the fundamental HE_{11} mode is thus required. The reflectivities of a DBR and a metal mirror were analyzed in Ref [37]. for a low-diameter GaAs nanowire. It was shown that the small diameter results in strong diffraction effects in the DBR mirror leading to poor reflectivity. On the other hand the metal mirror provides good reflection in the entire diameter regime. A weakness of the metal mirror is the coupling to surface plasmon polaritons propagating in the transverse plane. This coupling

results in a lowering of the reflectivity, but can be avoided by adding a thin intermediate dielectric layer between the nanowire and the metal. The effect of this layer is to perturb the condition for plasmon coupling while maintaining the high reflectivity coefficient of the GaAs-metal interface. The metal mirror is illustrated in Fig. 3(a).

The optically pumped photonic nanowire demonstrated in [28] employed silica for the dielectric layer. However, for electrical pumping a conducting dielectric material is required, and a transparent conducting oxide such as ITO is a natural choice.
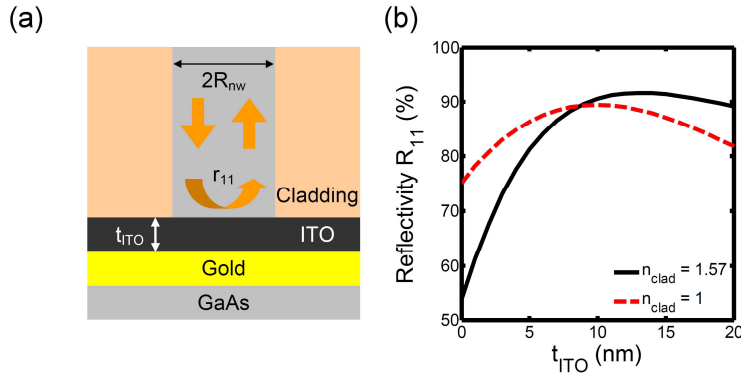

Fig. 3. Sketch of element II (a) and reflectivity $R_{11} = |r_{11}|^2$ of the HE_{11} mode (b) as function of ITO bottom contact thickness t_{ITO} for polymer and air claddings.

The reflection coefficient $R_{11} = |r_{11}|^2$ of the fundamental HE_{11} mode is shown in Fig. 3(b) as function of the thickness t_{ITO} of the bottom ITO layer. In the absence of the intermediate ITO layer, the reflectivity is only ~56 - 60% due to coupling to surface plasmon modes [37]. For large values of t_{ITO}, the value of R_{11} drops due to diffraction and destructive Fabry-Perot effects. We observe maximum modal reflectivity coefficients of ~89.5% and ~91.6% for air and polymer claddings, respectively. These values are rather close to the plane-wave reflection coefficient of 94.7% for a GaAs-gold interface under normal incidence conditions.

As long as the thickness of the gold layer is sufficiently large to prevent tunnelling of light into the GaAs substrate, the exact thickness does not influence the reflectivity and should instead be chosen to ensure good electrical conductivity.

Element III-A: Top conical tapering

Even though most of the photons are propagating towards the top of the nanowire, a low divergence of the output beam is necessary to ensure a high collection efficiency of the detection optics. The far field emission profile is related to the Fourier transform of the mode profile, and for small nanowire radii the far field profile is wide leading to a low γ. In our earlier work [38] we proposed to improve γ by implementing the conical tapering sketched in Fig. 4(a).

The tapering has two beneficial effects. First, it serves to adiabatically expand the fundamental mode such that the divergence of the output beam profile is reduced. Second, the mode is expanded into the air cladding and the reflection at the semiconductor-air interface is strongly reduced.
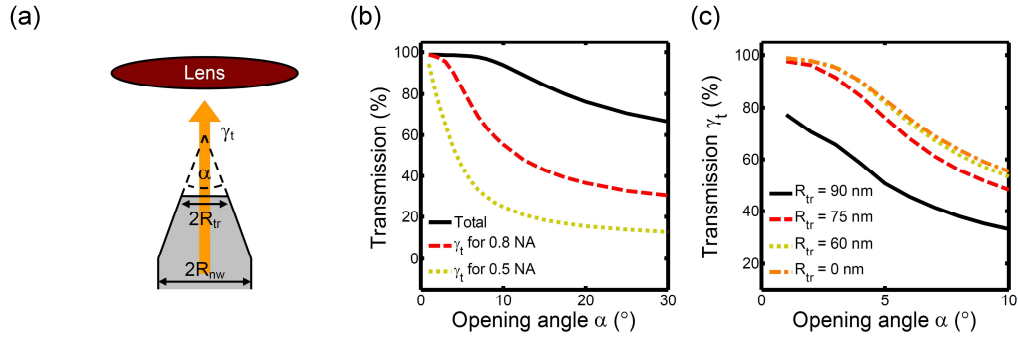
Fig. 4. Sketch of element IV-A (a) and total transmission and relative collection efficiency γ_t for 0.5 and 0.8 NA lenses (b) as function of opening angle α for a perfectly sharp tip. Relative collection efficiency γ_t for a 0.8 NA lens (c) as function of α for various values of R_{tr}. $R_{nw} = 110$ nm.

The total transmission into free space as well as the relative collection efficiency γ_t for 0.5 and 0.8 numerical aperture (NA) lenses are illustrated as function of taper opening angle α in Fig. 4(b) for a perfectly sharp tip, characterized by a truncation radius $R_{tr} = 0$, see Fig. 4(a). Here, the total transmission and γ_t are both normalized to the power of the forward propagating guided mode at the interface of elements III and IV. For large opening angles, the transition through the tapering is not adiabatic and the relative collection efficiency γ_t is low. For an adiabatic transition a small opening angle is required, and we observe that $\gamma_t \rightarrow 1$ as the opening angle α is decreased.

Obviously, a small α leads to a long tapering section and for this reason we also study the collection efficiency of a truncated taper. We have computed the collection efficiency γ_t as function of opening angle α for four truncation radii R_{tr}, and the results are shown in Fig. 4(c). We observe that for $R_{tr} = 90$ nm, γ_t is poor, however for a truncation radius R_{tr} of 75 nm the collection effiency is much improved and for 60 nm, γ_t is almost identical to that for the perfectly sharp tip. A truncation parameter of $R_{tr} = 60$ nm thus allows a reduction of the tapering height by a factor of two while maintaining the good collection efficiency.

Element III-B/C: Inverted tapering section

In all three designs a low divergence of the output beam is required to maintain a high collection efficiency. Whereas a conical taper is employed to adiabatically expand the mode into air in design A, designs B and C feature an inverted tapering which instead expands the mode inside the GaAs nanowire. The tapering sections are sketched in Figs. 5(a) and 5(d). The bottom radius R_{nw} is fixed at 110 and 120 nm for designs B and C respectively.

We first study the transmission coefficient γ_t of the fundamental HE_{11} mode as function of sidewall angle θ for various values of R_{top} for polymer and air claddings. The results are given in Figs. 5(b) and 5(e). Inspecting the figures, we observe two distinct domains. For a sidewall angle θ below ~5°, the transmission is near-adiabatic with values of γ_t above 95%, whereas an oscillatory behavior of the transmission for θ above ~5° is observed. For a fixed angle, the taper height h increases with R_{top} and due to the free-carrier scattering loss the transmission generally deteriorates for increasing R_{top}. We are mainly interested in the near-adiabatic regime for $\theta < 5°$, where the value of γ_t is above ~95%. Generally, a decreasing sidewall angle results in an improved adiabatic transition and a increasing transmission, however for $\theta \rightarrow 0$ the taper height h becomes substantial and the free-carrier absorption loss then reduces the transmission. We observe that the optimum transmission is obtained for sidewall angles between ~2° and 5°.
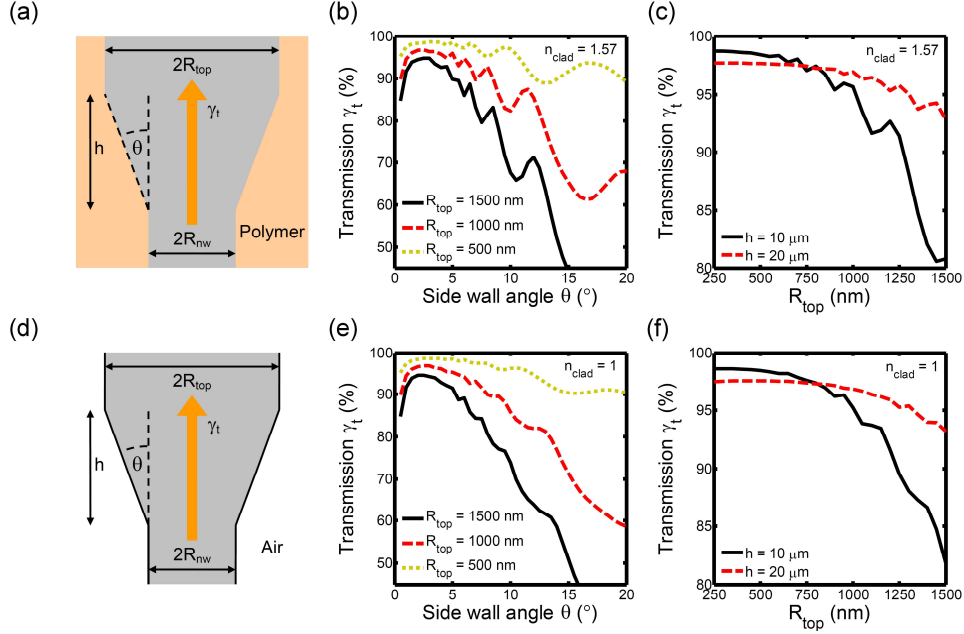
Fig. 5. Sketch of element III-B (a) and III-C (d). Transmission γ_t of the fundamental HE_{11} mode as function of sidewall angle θ for various values of R_{top} for polymer cladding (b) and air cladding (e). Transmission γ_t as function of R_{top} for $h = 10$ and 20 μm for polymer cladding (c) and air cladding (f).

In Figs. 5(c) and 5(e) we study the transmission as function of R_{top} for two fixed taper heights h of 10 and 20 μm. For a small $R_{top} < 750$ nm, the smaller taper height, $h = 10$ μm, leads to a smaller absorption loss and a slightly higher transmission than for $h = 20$ μm. On the other hand, for $R_{top} > 750$ nm, the side wall angle of the taper becomes large enough to compromise the adiabaticity of the fundamental mode transition. For small values, the side wall angle θ is given by $\theta \cong (R_{top} - R_{nw})/h$ and the larger taper height $h = 20$ μm results in a smaller side wall angle, a better preservation of adiabaticity and an improved transmission in the regime $R_{top} > 750$ nm.

Element IV-A: Side ITO contact

The fourth element in design A is the side ITO contact placed on top of the polymer cladding shown in Fig. 6(a) below. The contact is used to provide electrical pumping of the QD, however its influence on the optical mode should be minimized. To examine this influence we have computed the transmission γ_c of the HE_{11} fundamental mode through the contact section as function of ITO layer thickness t_{ITO} and of nanowire radius R_{nw}. The results are presented in Fig. 6(b).

For small R_{nw} the mode is predominantly situated outside the nanowire. In the absence of the ITO layer the transmission coefficient γ_c drops towards the plane-wave value for the polymer-air interface as $R_{nw} \to 0$, and the addition of the ITO contact further deteriorates this transmission. For large R_{nw} the confinement to the nanowire is strong. When R_{nw} increases, the influence of the cladding variation on the mode propagation decreases and the transmission approaches 100%. For $R_{nw} = 110$ nm we observe that γ_c is above 95% for all three ITO contact thicknesses considered. At this small radius the HE_{11} field profile has some overlap with the cladding but not enough to severely compromise the transmission. Also, the figure reveals that even a fairly thick ITO layer only reduces γ_c by ~2%. The exact thickness of the ITO contact is thus not a critical issue in fabrication. We note that for $R_{nw} = 110$ nm and $t_{ITO} = 50$ nm, the transmission γ_c is ~97.7%.
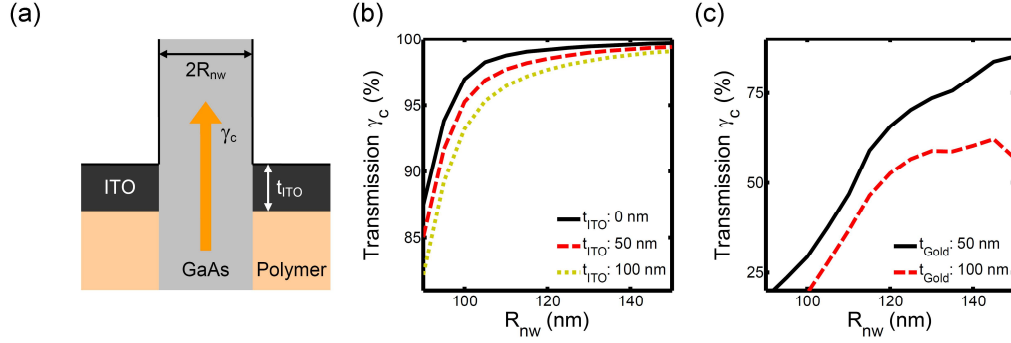
Fig. 6. Sketch of element III-A (a). Transmission γ_c of the fundamental HE_{11} mode through contact section as function of R_{nw} for various side contact thicknesses for an ITO contact (b) and a gold contact (c).

To justify our material choice of ITO for the side contact in element IV-A, we consider the transmission through the corresponding element with a side contact made of gold instead of ITO. The transmission for this gold contact is shown in Fig. 6(c). We observe that for R_{nw} = 110 nm, the transmission is below 50% for both contact thicknesses considered. This poor transmission is due to the HE_{11} mode extending into the gold cladding and experiencing strong absorption and scattering by the metal. Thus, the implementation of an ITO contact instead of a gold contact improves the total efficiency ε of the SPS by a factor of 2.

Element IV-B/C: Top ITO/gold contacts

In design B the top ITO contact serves two purposes, it allows for electrical pumping and it also serves as an anti-reflection (AR) coating to reduce the reflection from the semiconductor-air interface. The top contact element is sketched in Fig. 7(a). The thickness of the ITO contact layer is fixed at the AR optimum of one-quarter optical wavelength in bulk ITO, and we have computed the total transmission and relative collection efficiency γ_c for 0.5 and 0.8 NA lenses as a function of nanowire top radius R_{top}. The results are illustrated in Figs. 7(b) and 7(c) for polymer and air claddings. The total transmission and the collection efficiency γ_c are, as before, normalized to the power of the forward propagating mode at the interface between elements III and IV. We observe that for R_{top} ~110 nm, the transmission is less than 30% for both lenses. This low transmission is caused by the narrow HE_{11} mode waist resulting in a wide far field emission profile.

To achieve a high collection efficiency, the HE_{11} mode waist should be extended and for this reason we introduce the inverted tapering section described above. The real part 1.75 of n_{ITO} is close to the ideal AR coating index of sqrt(3.54) $\cong$ 1.88, however as R_{top} increases the total transmission approaches an upper bound of ~95% rather than 100% due to the weak material absorption of the ITO contact. As R_{top} increases, the collection efficiency is improved, however we keep in mind that a large top nanowire radius requires a long inverted tapering section.

The top gold contact element IV-C for design C is illustrated in Fig. 7(d). A gold contact ring similar to that used to electrically pump micropillars in Refs [7,39]. provides electrical current and Si_3N_4 is used in the central part as an AR coating. Again, the thickness of the AR coating is chosen to be one-quarter optical wavelength in bulk Si_3N_4 material. The collection efficiency γ_c for this element is given in Figs. 7(e) and 7(f) as function of R_{top} and the contact ring overlap parameter d for polymer and air claddings. We observe that for R_{top} = 750 nm the efficiency γ_c is above 85% and approaches ~99% for R_{top} approaching 1500 nm for all values of d considered. For the value R_{top} = 1500 nm, the overlap of the HE_{11} mode with the contact ring is so small that the influence on the collection efficiency is negligible.
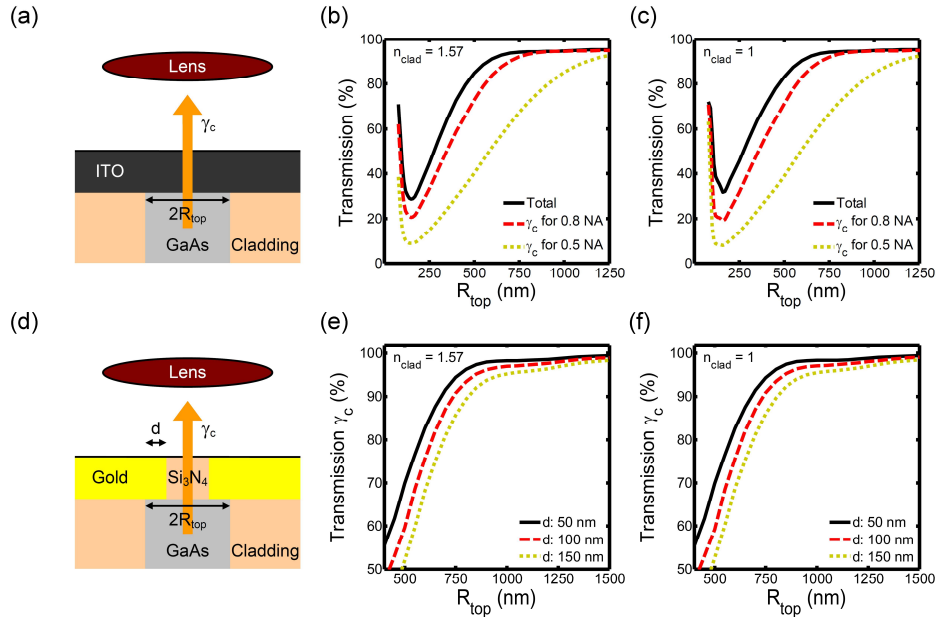
Fig. 7. Sketch of element IV-B (a) and total transmission and relative collection efficiency γ_c for 0.5 and 0.8 NA lenses as function of R_{top} for polymer (b) and air (c) claddings. Sketch of element IV-C (d) and relative collection efficiency γ_c for a 0.8 NA lens as function of R_{top} for various values of d for polymer (e) and air (f) claddings.

The refractive index of 1.99 of Si_3N_4 results in a maximum 1D plane-wave transmission coefficient of the AR coating of 99.7%. However an ideal AR coating with an index of ~1.88 and a transmission of 100% can be realized using silicon oxynitride SiON [35], which allows for an arbitrary composition-dependent refractive index between 1.45 and 2.

5. Fabrication issues

In the following, we briefly discuss the feasibility of fabricating the tapering sections III-A and III-B/C. These sections represent the most challenging part in the experimental realization of the proposed SPS designs, and we present initial fabrication results to demonstrate that the successful fabrication of the structures is indeed realistic.
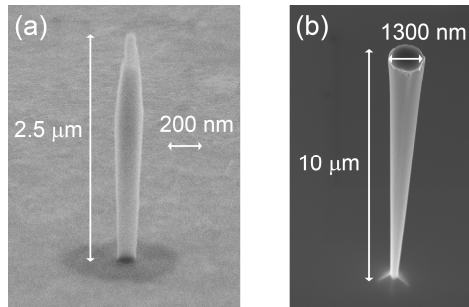

Fig. 8. Scanning-electron micrographs of regular conical tapering (a) featuring an opening angle α ~5° and inverted tapering section (b) with a side wall angle θ ~3°.

The fabrication of an optically-pumped SPS featuring a top taper of the III-A type has been demonstrated in Ref [28]. The associated process begins with an e-beam lithography step followed by a reactive ion etching step (SF_6 plasma) that define a conical Si_3N_4 hard-mask. This conical shape is then transferred into the GaAs layer, using another reactive ion etching step ($SiCl_4$-Ar plasma). Finally, the sidewall angle transferred in GaAs is the initial angle of

the Si_3N_4 mask divided by the GaAs-Si_3N_4 selectivity of the last etching step. This process has allowed reaching an opening angle α ~5°. A typical SEM picture is shown in Fig. 8(a): note that due to the presence of a lateral passivation layer deposited during the etching, the exact shape of the high-refractive index GaAs core is not accessible on such a picture. In the future, further improvements of the process may lead to a decrease of the tapering angle, resulting in a higher γ.

Following a similar process with different etching parameters, it is also possible to fabricate type III-B/C tapers. The sidewall angle is then directly controlled by the etching parameters. Figure 8(b) shows that structures featuring a 10 µm height and a sidewall angle θ ~3° are already achievable. Such parameters are close to the ones discussed in this paper. Experimental work is on-going to further optimize the process and obtain a wider top facet and further details of the associated fabrication process is beyond the scope of this paper.

Regarding design C, the air pocket could be defined with the following process. After planarization of the sample with a polymer and deposition of the top ring contact and contact pad, the polymer is etched with a highly selective dry etching step (O_2 plasma). The contact pad and the top facet of the wire will act as an etching mask, and a slight chemical component in the etching can be used to under-etch the polymer, to define an air pocket around the photonic wire.

6. Discussion of efficiency

With the various element coefficients β, r_{11}, γ_t and γ_c computed, we can now estimate the total efficiency of the proposed electrically-pumped SPS designs. The optimum parameters for the bottom part of the designs are fixed and summarized in Table 2. However we have the liberty of choosing α, R_{tr} and t_{ITO} in design A and R_{top}, h (or θ) and d in designs B and C. In the following we have chosen R_{tr} = 60 nm, t_{ITO} = 50 nm and d = 100 nm, and we study the total efficiency as function of the remaining free parameters. The QD is positioned 261 nm (269 nm) above the metal mirror in design B (design C) in an antinode of the field such that $\varphi = 0$.

Table 2. Element coefficients.

Parameter	Design A	Design B	Design C
β	83.3%	83.3%	96.3%
R_{nw}	110 nm	110 nm	120 nm
Mirror reflectivity R_{11}	91.6%	91.6%	89.5%

The total SPS efficiency ε as function of opening angle α for design A for a 0.5 and a 0.8 NA lens and as function of R_{top} for designs B and C for the taper heights h = 10 µm and h = 20 µm is given in Fig. 9. The results of calculations using the element-splitting model as well as results from exact computations are shown.

Inspecting Fig. 9(a) we observe that for the experimentally realistic opening angle of α = 3°, the total efficiency ε for design A is ~82% for the 0.8 NA lens. Good agreement between the results obtaining using the simplified model and those from a full computation is observed, validating the element-splitting approach. A small oscillatory deviation for the 0.8 NA curves is observed, which we attribute to an increasing reflection of the HE_{11} mode reaching the element III-A as the opening angle α is increased. This reflection is not taken into account in the simplified model.

For design B, Fig. 9(b) shows that the efficiency ε increases with R_{top} towards a maximum value of ~81% obtained for a top nanowire radius R_{top} of ~800 nm for the 0.8 NA lens. At this radius, the collection efficiency γ_t for the element IV-B is no longer improved by increasing R_{top} and the total efficiency ε clamps.

A similar behavior is observed in Fig. 9(c) where the efficiency ε for design C increases towards 89% as obtained for R_{top} ~900 nm. Figure 7(f) reveals that the collection efficiency γ_c for the element IV-C is slightly improved for R_{top} approaching 1500 nm, however for R_{top} > 750 nm the taper transmission coefficient γ_t starts to drop. There is thus a trade-off, between a large R_{top} to provide a high collection efficiency and a small R_{top} to maintain a high transmission through the inverted taper. For our choice of parameters the optimum value is ~900 nm for h = 20 µm.
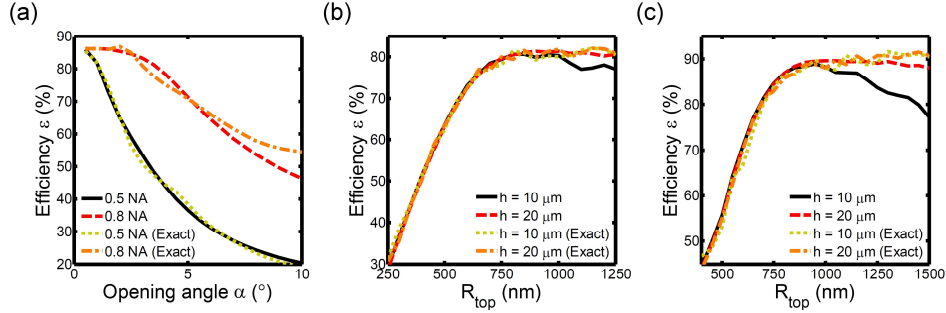
Fig. 9. SPS efficiency ε for design A (a) as function of opening angle α for 0.5 and 0.8 NA lenses. SPS efficiency ε for designs B (b) and C (c) as function of R_{top} for a 0.8 NA lens. Results from the simplified model and the exact computation are shown.

In both Figs. 9(b) and 9(c) we observe a slight deviation for $R_{top} > 750$ nm for the $h = 10$ µm curves computed using the simplified and the exact models. For design C, the efficiency obtained by the exact model actually increases beyond 89% as R_{top} approaches 1500 nm, whereas ε for the simplified model clearly decreases, reflecting the drop in transmission observed in Fig. 5(f) for R_{top} approaching 1500 nm. This discrepancy can be understood by considering the breakdown of the adiabatic transition of the HE_{11} mode as it propagates through the inverted taper. For a fixed taper height h, the side wall θ increases with R_{top} and for $R_{top} > 1000$ nm there is significant coupling to higher order modes HE_{1m} ($m > 1$). In the simplified model this coupling is treated as a loss, however even though these higher order modes generally have a more divergent far field emission profile, a significant part of the light from these modes can be picked up by the 0.8 NA lens. In this multi-mode picture, the break-down of adiabaticity means that the power initially carried by the HE_{11} mode is distributed over various HE_{1m} modes at the top part of the taper, and for sufficiently large values of R_{top} all this power is still coupled to the lens. Depending on the application, this distribution of power among several HE_{1m} modes may, or may not, be acceptable. E.g. if subsequent coupling to a single-mode fiber is required, the power in the higher order modes will be lost and the efficiency ε will be correctly predicted by the simplified single-mode model presented here.

We have chosen parameter values based on initial fabrication tests and it is not yet completely clear which values for the parameters α, R_{trunc}, t_{ITO}, h, R_{top} and θ can be achieved in the fabrication of the complete structures. However, we can estimate the upper bounds of the efficiency under the assumption that arbitrary geometric parameters are possible. All three designs are limited by their β factor and the reflection coefficient R_{11} of the bottom mirror. Furthermore, the designs are limited by the transmission through their respective contact elements. This results in an upper bound of 86.7% for the design A. Neglecting absorption loss in the inverted taper due to free carrier scattering, the corresponding bounds are 84.3% and 95.5% for designs B and C respectively.

The design C benefits from the high β value of 96.3% due to the large GaAs-air index contrast and a transmission of 99.7% in the plane-wave limit through the Si_3N_4 AR coating. The main bottlenecks for the total efficiency for design C are thus absorption losses in the inverted taper and the reflectivity coefficient of 89.5% of the metal mirror. The absorption losses may be reduced by carefully optimizing the doping profile of the inverted taper. The reflectivity of the metal mirror is limited by the plane-wave reflection coefficient of 94.7% for the GaAs-gold interface. Even though this coefficient can be slightly increased by replacing gold with silver, a DBR mirror is most likely necessary to obtain 100% reflectivity. A regular DBR mirror performs poorly at small nanowire diameters [26], however the mode-matched DBR structure presented in [44] could be considered. This element represents a substantial design complication and a thorough analysis is outside the scope of this paper.

Finally, we discuss the possibility of non-ideal carrier-capture efficiency, that could in turn contribute to the upper limit on ε. In Ref [7], values of ζ between 20% and 72% were reported

for micro-cavity devices. These low values were attributed to non-radiative recombination at the sidewalls and associated carrier losses. This effect can in principle be compensated by the injection of a stronger current. However, in the micro-cavity case, this solution is not ideal due to the marked degradation of the $g^{(2)}$ as the pumping current increases. The photonic nanowire SPS has demonstrated a nearly perfect $g^{(2)}$ at saturation of the X transition, under non-resonant optical pumping [28]. Thus, it is likely that a stronger current up to X saturation is possible in an electrically pumped device, without the burden of detrimental multi-photon pulses. Another solution proposed in [7], which is not specific to photonic nanowires is the passivation of the sidewalls. This helps to decrease non-radiative recombination at weak currents, as demonstrated successfully in the context of electrically pumped lasers based on nanocavities [45].

7. Conclusion and outlook

We have proposed and analyzed three electrically-pumped SPS structures. The designs are based on a GaAs nanowire with an embedded QD and on ITO and gold contacts. The operating principle ensuring a high β relies on a geometrical screening of radiation modes rather than the Purcell effect. This choice avoids the high sensitivity to geometry imperfections, which limits the efficiency of traditional high-Q cavity-based SPS designs.

The various elements of the designs have been analyzed and the influence of geometrical parameters on the efficiency has been quantified. For realistic geometrical parameters we predict the total efficiencies of the designs A, B and C to be 82%, 81% and 89% respectively. These values are well above reported values for state-of-the-art electrically-pumped SPS's based on cavity effects. For all the designs, the tapering sections are critical elements, and we have demonstrated the feasibility of experimental fabrication of both the top conical and the inverted tapering. We have discussed possible strategies for further increasing the total efficiency towards 100%.

Finally, some advanced applications of SPS (such as quantum computing using single photon Qbits) require single photon indistinguishability, which is possible only if the emitter's dephasing time is limited by the SE time. Although SE enhancement using the Purcell effect is, generally speaking, favorable to reach this regime, we note that the emission for indistinguishable photons has already been demonstrated for electrically driven QD devices in the absence of measurable Purcell effect [46,47]. Also, "fast" emitters such as QDs in the giant-oscillator strength regime [48] or donor impurities [49] are good candidates for the generation of indistinguishable photons without the help of cavity effects. Embedding such emitters in photonic wires appears therefore as a promising route toward efficient and practical sources of indistinguishable single photons.

Acknowledgments